Nano Research

Open Access

Research Article

Ce-UiO-66 nanozymes with charge-regulated uricase-like activity for enzyme/reagent-free detection of uric acid

Zhixiong Guo[1,§], Da Chen[1,§], Wei Gao[2]✉, Yongquan Qu[1]✉, and Zhimin Tian[1]✉

[1] *Key Laboratory of Special Functional and Smart Polymer Materials of Ministry of Industry and Information Technology, School of Chemistry and Chemical Engineering, Northwestern Polytechnical University, Xi'an 710054, China*
[2] *State Key Laboratory of Solidification Processing, Center for Nano Energy Materials, School of Materials Science and Engineering, Northwestern Polytechnical University, Xi'an 710072, China*
[§] *Zhixiong Guo and Da Chen contributed equally to this work.*

Cite this article: *Nano Research*, **2025**, *18*, 94907115. https://doi.org/10.26599/NR.2025.94907115

ABSTRACT: Designing highly performed uricase-like nanozymes through enzymatic-like colorimetric analysis system is of vital significance for the quantitative detection of uric acid (UA). Herein, series of Ce-UiO-66 nanozymes with different surface charges through the ligand engineering strategy were rationally designed and synthesized as efficient uricase mimics with tailorable uricase-like activities to catalytically convert UA into allantoin and H_2O_2. Importantly, by tuning the functional groups of 1,4-benzoic acid ligands, we explored the relationships between the surface charges of Ce-UiO-66-X (X = H, NO_2, Br, CH_3, and OH) nanozymes and their uricase-like activity. Among them, Ce-UiO-66-CH_3 with the moderate surface charge exhibited optimal substrate adsorption and product desorption, displaying the highest uricase-like activity. Significantly, H_2O_2, as the product of UA oxidation, enabled Ce-UiO-66-CH_3 itself as a dose-dependent chromogenic substrate of H_2O_2, giving a white-to-orange color evolution due to the Ce-UiO-66-CH_3-to-CeO_2 phase transition. Afterwards, a smartphone-assisted all-in-one enzyme/reagent-free biosensor based on Ce-UiO-66-CH_3 was established for the precise visual detection of UA analysis, which was featured by a wide detection range (31–4000 μM), a high sensitivity (limit of detection: 8.9 μM), a rapid response (~ 3 min), a high structural stability, and a high anti-interference ability.

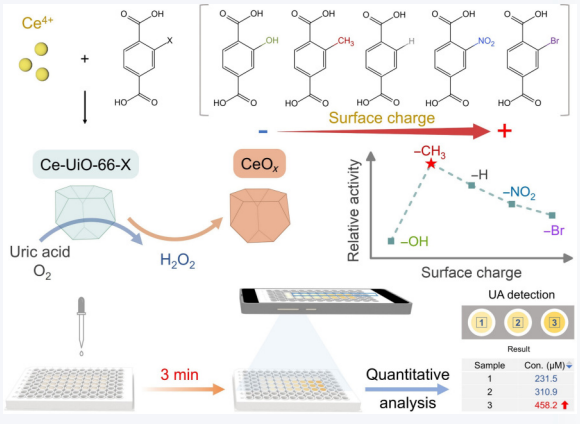

KEYWORDS: Ce-UiO-66, uricase-like nanozyme, colorimetric uric acid analysis, enzyme/reagent-free detection, smartphone

1 Introduction

Uricase, which is widespread in microorganisms, plants, and majority of animals, specifically catalyzes the oxidation of uric acid (UA) with a low solubility in physiological environments into molecules (i.e., allantoin) with a high solubility and excretion [1–3]. However, humans and hominoid apes are lack of the uricase. When the UA levels are elevated, the excessive UA cannot be effectively eliminated, leading to hyperuricemia and further triggering numerous diseases (hypertension, cardiovascular diseases, diabetes, uric acid renal stones, gouty arthritis, etc.) [3–7]. Hence, the uricase and uricase-loaded nanocomposites have been widely utilized for the UA-related biocatalytic and biomedical applications, including various methods for the UA analysis and gout treatments [8–10]. Nevertheless, natural uricase generally suffers from many serious intrinsic limitations for scale-up biomedical applications, such as low yields, poor stability, high costs, and immunogenicity that can cause severe allergic reactions, necessitating the pursuit of effective alternatives to overcome these drawbacks [9, 10].

Recent advances in nanozymes with the uricase-like activity have shown considerable promises for potential application due to their high stability, low price, abundance of editable sites, and excellent biocompatibility [11–15]. Specifically, MnO_2, Fe-based nanozyme, noble metals, atomically dispersed Ni atom, and metal organic

Received: September 25, 2024; **Revised:** October 31, 2024
Accepted: November 3, 2024

✉Address correspondence to Wei Gao, wei.gao@nwpu.edu.cn; Yongquan Qu, yongquan@nwpu.edu.cn; Zhimin Tian, zhimintian@nwpu.edu.cn

frameworks (MOFs) were found to display uricase-like activity [16–26]. Despite those strategies by using various catalysts with uricase-like activity for biomedical applications, the enzyme-mimic catalytic mechanisms and structure–activity relationship of those nanozymes behind these strategies are rarely explored. Meanwhile, it is of great significance to investigate the reaction mechanism of their uricase-like activity and understand the correlation between their surface properties and uricase-like activity, thereby realizing rational design and achieving excellent activity for the UA-related diseases diagnosis and treatments.

As a specific type of heterogeneous catalysts, nanozymes are interdisciplinary of two critical fields: heterogeneous catalysis and enzymology [27–30]. In a typical enzyme-like catalytic process, the reaction steps include the substrate adsorption, activations of reactants on the catalyst surfaces, and product generation/desorption, similar to the elementary steps of heterogeneous catalysts [30–34]. Besides, the enzyme-like catalytic activity of nanozymes is commonly evaluated by the Michaelis–Menten kinetics, in which the kernel parameter of Michaelis constant (K_m) is used to describe the adsorption affinity of substrates on the surfaces of nanozyme catalysts [16, 29, 30, 34]. Hence, exploring the catalytic mechanisms of uricase-like nanozymes through surface science is essential in the ingenious design and regulation of nanozymes with higher activity and intelligent multifunction [31–34].

Recently, as a type of emerging nanozymes, MOF-based nanozymes have received considerable attention in disease therapeutics and biochemical analysis due to their large surface area, controllable sizes, ordered chemical structure, and tunable surface properties [35–37]. Meanwhile, among the numerous nanozymes, the cerium-based nanozymes have shown well application prospects in biomedicine [38–46]. Our group previously reported a sensitive and reagent-free colorimetric analysis platform for one-step detection of various biomarkers by integrating natural oxidase with Ce-UiO-66 as the enzyme immobilization carrier and chromogenic [47]. Herein, Ce-UiO-66 itself was found to possess uricase-like activity by catalytically convert UA into allantoin and H_2O_2 within a wide pH environment (6–12).

Through ligand engineering strategy to modulate the surface charge of series of Ce-UiO-66-X with various functional groups (X = H, NO_2, Br, CH_3, and OH) in 1,4-benzoic acid ligands, Ce-UiO-66-CH_3 exhibited the highest uricase-like activity (Scheme 1). Hence, Ce-UiO-66-CH_3 alone as both the uricase-like nanozyme and chromogenic reagent was demonstrated as rapid and sensitive UA biosensors, featured by all-in-one enzyme/reagent-free colorimetric detection with great advantages over the common ones based on natural uricase, peroxidase and unstable chromogenic agent (3,3',5,5'-tetramethylbenzidine, 2,2'-azino-bis(3-ethylbenzothiazoline-6-sulfonic acid, etc.) [47–49]. Afterward, a smartphone-assisted colorimetric detection system based on Ce-UiO-66-CH_3 exhibited a wide linear response range of 31 to 4000 μM and a low limit of detection (LOD) of 8.9 μM for the stable and rapid (3 min) detection of UA in urine. This work provides insights on the surface–activity relationships of Ce-UiO-66 nanozymes with uricase-like activity via modulating the surface charge, which show great potentials in clinical diagnosis.

2 Experimental

2.1 Synthesis of Ce-UiO-66

Ce-UiO-66 nanozymes were prepared by a wet chemistry method at room temperature [47]. Typically, disodium terephthalate

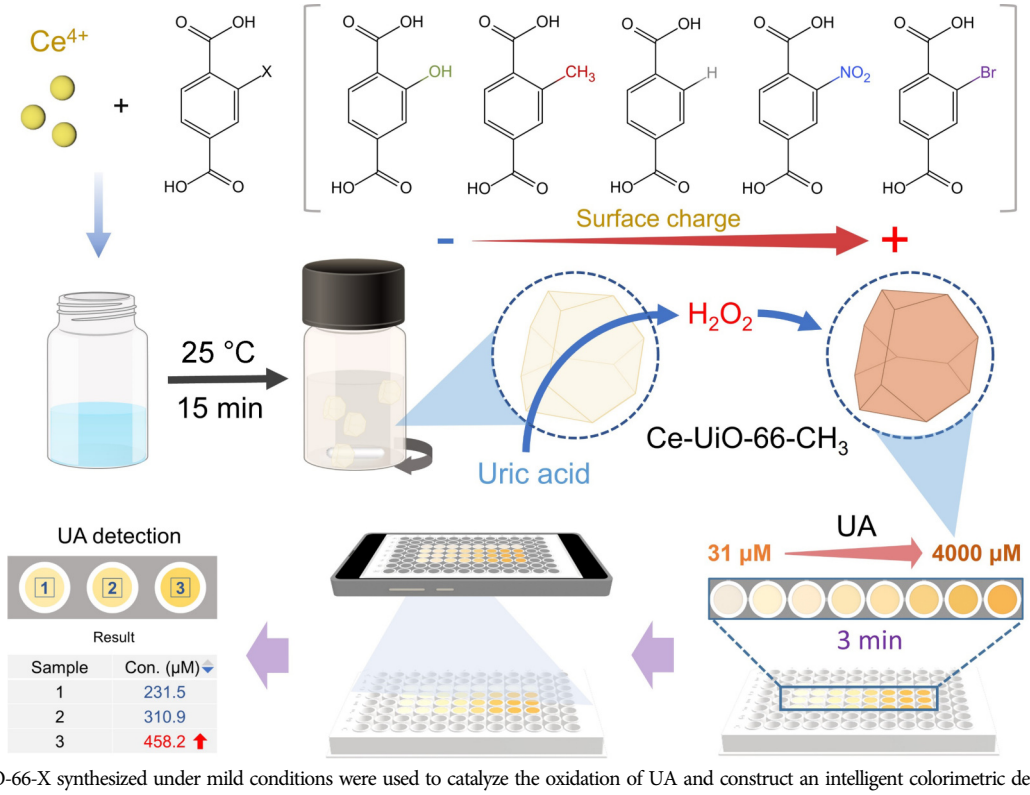

Scheme 1 Ce-UiO-66-X synthesized under mild conditions were used to catalyze the oxidation of UA and construct an intelligent colorimetric detection platform for UA.

(Na_2BDC,45 mg) and sodium acetate (100 mg) were dissolved in 1.2 mL of water (18.2 MΩ·cm). Next, 0.4 mL of an aqueous solution of cerium ammonium nitrate (117 mg) was added into the above mixture under stirring, accompanied with the production of Ce-UiO-66 as white powders. After 15 min, the white products were collected by centrifugation and washed with copious of water for three times. The Ce-UiO-66 was vacuum-dried at room temperature. Afterwards, Ce-UiO-66 was redispersed in water (4 mg/mL) and stored at 4 °C. Preparation of Ce-UiO-66-X (X = NO_2, CH_3, Br, and OH) was similar to that of Ce-UiO-66 except the usage of Na_2BDC with various functional groups.

2.2 Validation of uricase-like activity of Ce-UiO-66

Initially, 15 μL of aqueous Ce-UiO-66 solution (4 mg/mL) was loaded into a centrifuge tube (2 mL). Then, 1.445 mL of water was added into the tube. Afterwards, 40 μL of aqueous UA solution (4 mM) was introduced. The total volume of solution was fixed at 1.5 mL. The mixture was then stood for 5 min and centrifuged off. Finally, 1.0 mL of supernatant was transferred to a cuvette for analysis of the absorbance at 290 nm using a ultraviolet–visble (UV–vis) spectrophotometer. The entire process was repeated for three times in parallel to ensure the accuracy of measurements.

2.3 Catalytic mechanism of Ce-UiO-66

To verify the dependence of the uricase-like activity of Ce-UiO-66 on O_2, the uricase-like catalytic performance was performed under the air, N_2, and O_2 environments, respectively. The calculation equation was defined as follows

$$y = \left(\frac{A_{\mathrm{Ctrl}} - A_x}{A_{\mathrm{Ctrl}} - A_{\mathrm{air}}}\right) \times 100\% \quad (1)$$

where y represents the relative activity in each atmosphere, A_{Ctrl} is the UV–vis absorbance of UA at 290 nm before the reaction, and A_x denotes the UV–vis absorbance of UA at 290 nm after the reaction. The absorbance values of A_{air}, $A_{\mathrm{N_2}}$, and $A_{\mathrm{O_2}}$ correspond to the absorbance measured under air, N_2, and O_2 atmospheres, respectively.

2.4 Temperature and pH dependence analysis of Ce-UiO-66 and natural uricase

2.4.1 Temperature dependence analysis

Initially, 1.5 mL of UA solution (100 μM) was injected into a centrifuge tube (2 mL). The tube was submerged into a water bath for 5 min at the desired temperatures ranging from 0 to 60 °C. Then, 15 μL of Ce-UiO-66 (4 mg/mL) or natural uricase was introduced into the above solution. After 5 min, the solids in the tubes were centrifuged off. Then, 1.0 mL of the supernatant was transferred into a cuvette for analysis by measuring the absorbance at 290 nm with a UV–vis spectrophotometer. The entire process was repeated for three times in parallel to ensure the accuracy of measurements.

2.4.2 pH dependence analysis

Initially, 40 μL of UA solution (4 mM) was added into 1.445 mL of H_2O with various pH values ranging from 4 to 12. Then, 15 μL of Ce-UiO-66 (4 mg/mL) or natural uricase was injected into the above mixture. After 5 min, the solids were centrifuged off. Then, 1.0 mL of the supernatant was transferred into a cuvette for analysis by measuring the absorbance at 290 nm with a UV–vis spectrophotometer. The entire process was repeated for three times in parallel to ensure the accuracy of measurements.

2.5 Kinetic analysis of Ce-UiO-66 and natural uricase in the UA detection

The K_m is defined by Eq. (2)

$$\frac{1}{v} = \frac{K_m}{V_{\max}} \cdot \frac{1}{[S]} + \frac{1}{V_{\max}} \quad (2)$$

where v is reaction rate, $V_{\max}$ is maximum reaction rate, and $[S]$ is concentration of UA.

2.6 Colorimetric detection of Ce-UiO-66-CH_3

Typically, the Ce-UiO-66-CH_3 dispersion (0.36 mL, 0.5 mg/mL) was mixed with 20 μL of UA solution with different concentrations (30–4000 μM) in a 96-well plate. Then, the mixture was further incubated at room temperature for 3 min and a smartphone was used to record the color evolution of Ce-UiO-66-CH_3 in a dark environment. After that, the APP of Visual Detection was used to convert colorimetric images into RGB values (Video ESM1, RGB = red, green, and blue) [47]. For blue as the complementary color of orange, the intensity of the blue channel was employed to quantify the intensity of colors in the capture images, which was used to establish standard curves for the quantification of UA. For each concentration of UA, the measurements were repeated for three times.

2.7 Calculation of LOD

The LOD was calculated according to Eq. (3)

$$y_{\mathrm{LOD}} = y_{\mathrm{bg}} + 3\sigma \quad (3)$$

where y_{LOD} is the color intensity of LOD, y_{bg} is the color intensity of blank background, and σ is the standard error of y_{bg}.

2.8 Thermal and storage stability of Ce-UiO-66-CH_3

2.8.1 Thermal stability

Briefly, 0.36 mL of aqueous Ce-UiO-66-CH_3 solution (0.5 mg/mL) was added into a 96-well plate and pre-heated at the settled temperatures (0, 5, 37, 50, and 60 °C) for 30 min. After mixing with 20 μL of UA solution (4 mM) for 3 min at room temperature, the color intensity of each well was recorded by a smartphone and analyzed by the Visual Detection.

2.8.2 Storage stability

Initially, the aqueous suspension of Ce-UiO-66-CH_3 (0.3 mg/mL) was prepared. Then, 0.36 mL of stock solution was added into the selected wells of a 96-well plate and stored at 25 °C for desired periods. Then, 20 μL of UA solution (4 mM) was injected into the selected wells with the stock Ce-UiO-66-CH_3 suspension. After 3 min at room temperature, the color intensity of each well was recorded by a smartphone and analyzed by the Visual Detection.

2.9 Selectivity of the colorimetric platform

Various substances (KCl, $CaCl_2$, Na_2CO_3, $Mg(NO_3)_2$, $Zn(NO_3)_2$, $Pb(NO_3)$, glucose, sucrose, maltose, fructose, lactose, lysine, glycine, L-arginine, and histidine) were used to evaluate the UA-detection ability of Ce-UiO-66-CH_3 against the environmental interferences.

The concentrations of UA and interfering substances were controlled at 1 and 5 mM, respectively. The ability of Ce-UiO-66-CH_3 against those interfering substances was determined by comparing the color intensity in the absence of interfering substances (K_0) and the one in the presence of interfering substances (K). All measurements were performed for three times.

2.10 UA detection in serum samples

Fetal bovine serum (FBS) was employed to mimic the serum samples. Desired amounts of UA were added to FBS to reach the final concentrations of 125, 200, and 500 μM. Then, the accurate UA concentrations were quantified by using the Ce-UiO-66-CH_3 colorimetric platform and commercial kits (NJJCBIO, C012-1-1). After the results were obtained, the recovery rates were calculated. Each experiment was carried out for three times in parallel.

3 Results and discussion

3.1 Synthesis and characterization of Ce-UiO-66

The Ce-UiO-66 was synthesized by a facile one-pot process with Ce^{4+} as the metal ion, Na_2BDC as the organic ligand, and sodium acetate as the modulator at room temperature (Fig. 1(a)) [45]. As revealed from the transmission electron microscopy (TEM) image (Fig. 1(b)), as-synthesized Ce-UiO-66 possessed the irregular morphology of nanoparticles with a diameter of ~ 100 nm. The X-ray diffraction (XRD) pattern of Ce-UiO-66 was well consistent with the simulation of UiO-66, confirming the successful preparation of Ce-UiO-66 (Fig. 1(c)). To gain insight into its precise structure, the Fourier transform infrared (FTIR) spectrum of Ce-UiO-66 was analyzed (Fig. 1(d)). The C–O_2 characteristic

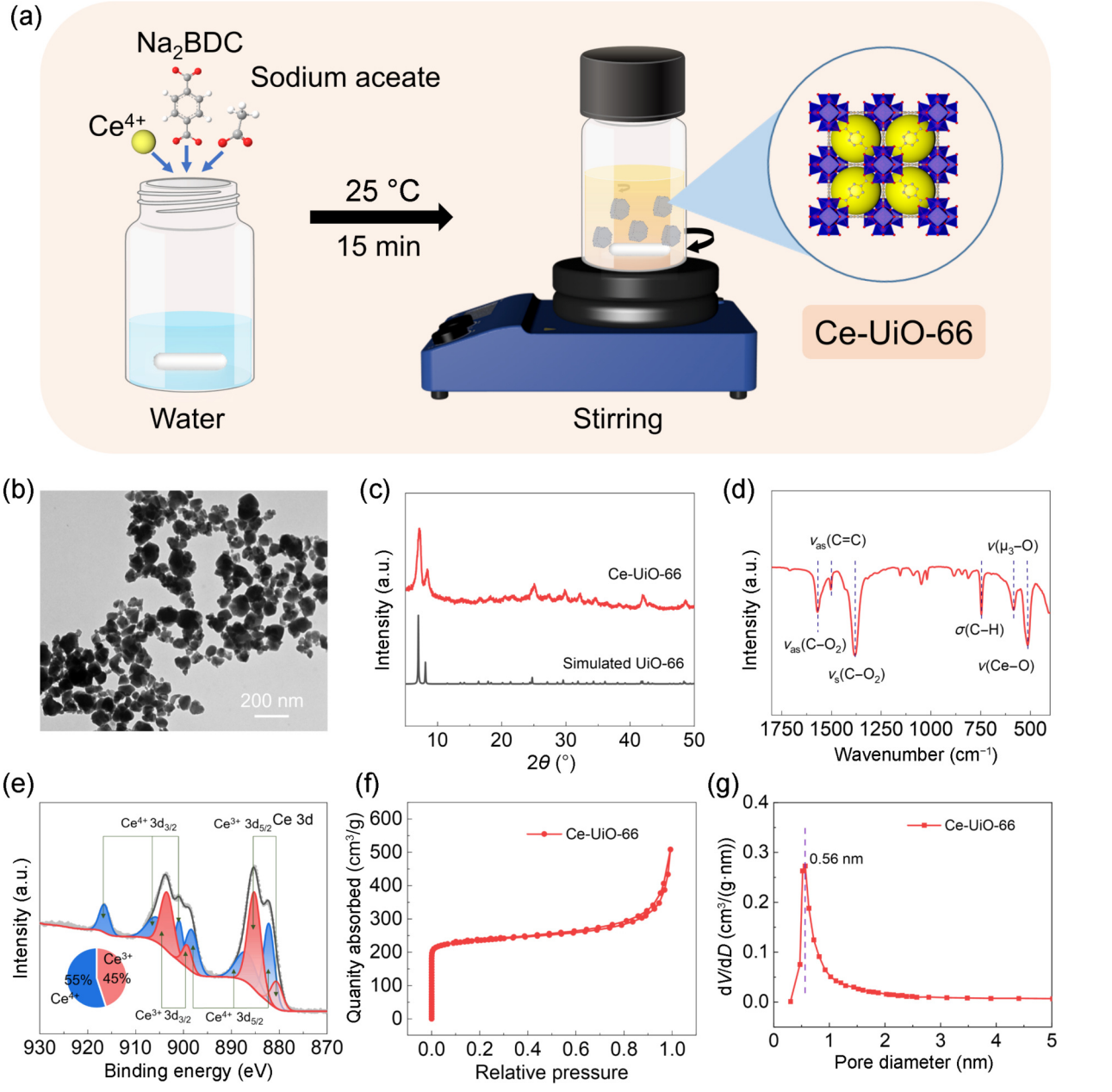

Figure 1 (a) Synthetic illustration of Ce-UiO-66. Characterizations of Ce-UiO-66: (b) TEM image, (c) XRD patterns, (d) FTIR spectrum, (e) XPS spectroscopy, (f) N_2 adsorption and desorption curves, and (g) pore size distribution.

absorption peaks at 1568 and 1385 cm^{-1} were attributed to the asymmetric stretching vibrations of the carboxyl group in the Na_2BDC ligand. The C=C at 1500 cm^{-1} was the characteristic vibration peak of aromatic ring. The characteristic peak at 748 cm^{-1} was assigned to the bending vibration of the C–H bond in the benzene ring. The peaks at 583 and 512 cm^{-1} correspond to the three-bridged oxygen μ_3–O stretching vibration and the stretching vibration of the Ce–O bond in Ce-UiO-66, respectively. These results indicated the successful synthesis of Ce-UiO-66.

Ce-UiO-66 was formed by alternately linking of $[Ce_6O_4(OH)_4]^{12+}$ and 12-fold BDC^{2-} to give the structural formula of $[Ce_6O_4(OH)_4(BDC)_6]$. Each Ce^{4+} center of $[Ce_6O_4(OH)_4]^{12+}$ cluster exhibits a square antiprismatic geometry with a composition of $[(\mu_3\text{-}O)_2(\mu_3\text{-}OH)_2(\mu_2\text{-}COO^-)_4]Ce$. X-ray photoelectron spectroscopy (XPS) was then performed to explore the oxidation states of metal ions in Ce-UiO-66. Notably, XPS analysis of Ce 3d indicated that cerium in Ce-UiO-66 was in a mixed valence state of 3+ and 4+, with a Ce^{3+} fraction of 45% (Fig. 1(e)). The abundant Ce^{3+} ratio of Ce-UiO-66 suggested that the introduction of the sodium acetate as modulator facilitated the generation of Ce^{3+} center, which was crucial for the catalytic performance of Ce-based MOF nanozymes, as well as for the UA oxidation [38–40]. Furthermore, Ce-UiO-66 exhibited the conventional type I N_2 adsorption and desorption isotherms, which were commonly observed on microporous adsorbents due to the filling of micropores (Fig. 1(f)). Determined by Brunauer–Emmett–Teller method, a large number of micropores with a diameter of about 0.56 nm were observed in Ce-UiO-66 with a specific surface area of 923 m^2/g (Fig. 1(g)). Hence, the high specific surface area and porosity of Ce-UiO-66 were conducive to expose active site, which was beneficial for the adsorption and conversion of UA [35–37].

3.2 Performance of Ce-UiO-66 as uricase mimic

Then, the uricase-like activity of Ce-UiO-66, including the UA oxidation and catalytic kinetics, was investigated by using UV–vis absorption spectroscopy.

The UV–vis absorption spectrum of UA showed its typical absorption peak at 290 nm (Fig. S1 in the Electronic Supplementary Material (ESM)) [50]. Therefore, the standard curve between the concentration of UA and the corresponded adsorption was established at the adsorption peak of 290 nm (Fig. S2 in the ESM). The UV–vis absorption spectra of UA (100 μM) after the oxidation catalyzed by Ce-UiO-66 (40 μg/mL) at different time in pure water are shown in Fig. 2(a). After mixing UA with Ce-UiO-66, the typical absorption peak of UA at 290 nm was reduced quickly within the initial 5 min. The FTIR analysis confirms the effective adsorption of UA on the surface of Ce-UiO-66, providing further evidence for the occurrence of the UA oxidation reaction (Fig. S3 in the ESM). The degradation ratio approached saturation after 120 min (Figs. 2(a) and 2(b)). By fixing the concentration of UA at 100 μM, the uricase-like activity of Ce-UiO-66 at 50 μg/mL was adopted for all analysis in this study due to its moderate reaction rate (Fig. S4 in the ESM). To assess the catalytic performance of Ce-UiO-66 in the oxidation of UA, we compared its activity with that of natural uricase across various temperatures and pH levels. The uricase-like activity of Ce-UiO-66 nanozyme was evaluated at various temperatures (5–60 °C) in media with various pH values (4.0–12.0). The uricase-like activity of Ce-UiO-66 was enhanced with temperatures increased from 4 to 25 °C (Fig. S5(a) in the ESM). Afterwards, the catalytic performance of Ce-UiO-66 approached a maximum activity with small fluctuations within the range of 25–60 °C. Meanwhile, the uricase-like activity of Ce-UiO-66 initially increased with the increase of pH values of reaction environments, reaching a high activity at pH of 7.0 and then remaining stable afterwards (Fig. S5(b) in the ESM). In contrast, the UA catalytic efficiency of natural uricase was significantly inhibited at pH values above 9 and temperatures of 50 °C, demonstrating the superior performance of Ce-UiO-66 over natural uricase in harsh environments [51, 52]. Compared with natural uricase, Ce-UiO-66

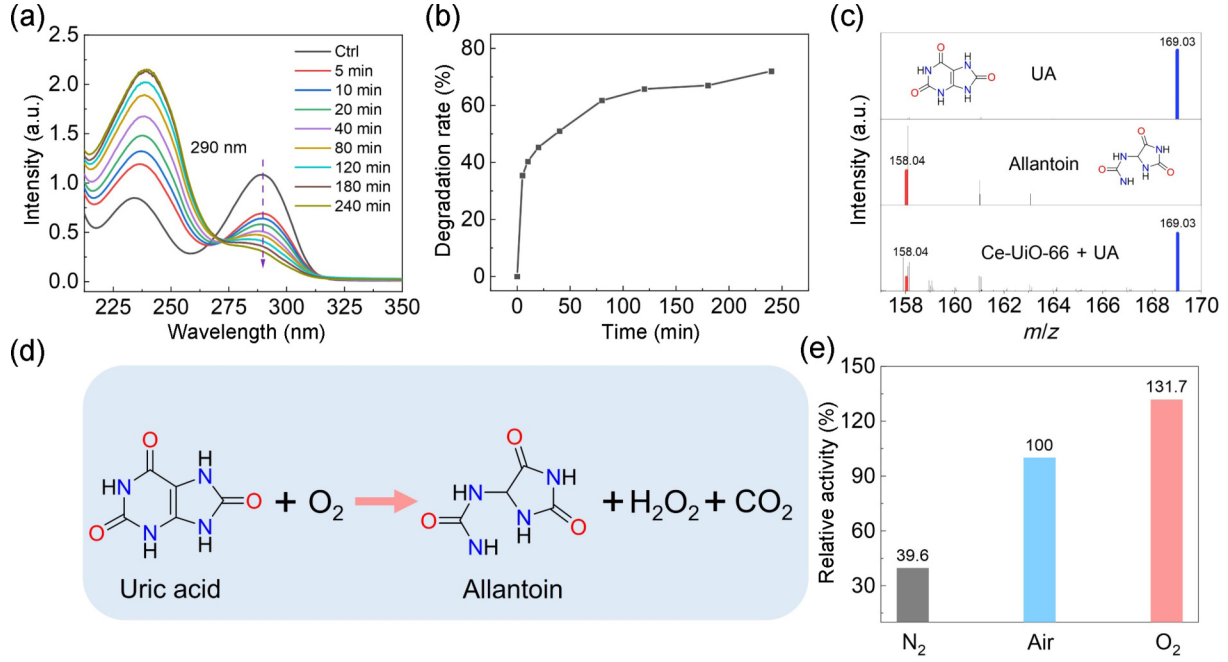

Figure 2 (a) UV–vis absorption spectra of the supernatant of the UA solution after the degradation catalyzed by Ce-UiO-66 at different time and (b) degradation rate curves. (c) HPLC-MS of standard UA and allantoin molecules and the chemicals in solution after colorimetric reaction. (d) Reaction pathway of the UA oxidation with Ce-UiO-66 as catalysts. (e) Relative activity of Ce-UiO-66 for catalyzing the UA oxidation in different gas atmospheres.

maintained efficient catalytic activity at higher temperatures under the medias with a wider pH range, suggesting its promising potentials for biomedicine applications in diverse physiological environments. Overall, the ultimate reaction conditions were optimized as 50 μg/mL of Ce-UiO-66, 100 μM of UA in pure water, reaction time of 5 min, and temperature of 25 °C.

Importantly, allantoin, the degradation product of UA, was successfully detected by the high-performance liquid chromatography-mass spectrometry (HPLC-MS) for Ce-UiO-66 (Fig. 2(c)), unambiguously demonstrating the uricase-like activity of Ce-UiO-66 through the pathway in Fig. 2(d). To further confirm the critical role of O_2 in the uricase-like reaction catalyzed by the Ce-UiO-66 nanozyme, the catalytic performance of Ce-UiO-66 was analyzed under various environments. As displayed in Fig. 2(e), the degradation of UA was significantly enhanced for the system saturated with O_2. Oppositely, the degradation ratio of UA was evidently reduced for the system saturated with N_2. The control experiments illustrated that O_2 involved the uricase-like reaction of Ce-UiO-66 and efficiently boosted the UA degradation.

Subsequently, we investigated steady-state kinetic data of Ce-UiO-66 and natural uricase. The Michaelis–Menten kinetics toward UA were observed for natural uricase and Ce-UiO-66 nanozyme. Figure 3(a) shows the relationship curves between the initial reaction rates and the UA concentrations. The K_m and maximum initial velocity (V_{max}) were then calculated by the Lineweaver–Burk plots of the double reciprocal of the Michaelis–Menten (Fig. 3(b)). As listed in Table S1 in the ESM, the K_m values of natural uricase and Ce-UiO-66 were 33.66 and 33.47 mM, respectively; and the V_{max} values of natural uricase and Ce-UiO-66 were 0.106 and 0.111 μM/s, respectively. The data illustrated that Ce-UiO-66 exhibited the similar affinity and catalytic efficiency for the UA degradation as natural uricase. Due to its higher stability, Ce-UiO-66 can be a viable substitute of uricase in catalyzing the oxidation of UA. Thus, Ce-UiO-66 exhibits the comparable uricase-like activity and superior stability under various physiological conditions, indicating its great potential as an alternative of natural uricase and laying a foundation for biological applications.

3.3 Effects of the surface charge on the uricase-like activity of Ce-UiO-66 nanozyme

As a typical surface catalytic process, the adsorption of the substrate and desorption of products could be affected by the surface charge of the nanozymes [30–33]. Hence, optimizing uricase-like activity through the modulation of surface charge can further improve the catalytic performance of the Ce-UiO-66 nanozymes. In this work, we tailored the surface charge to optimize the uricase-like activity of Ce-UiO-66 nanozymes through ligand engineering. The synthesis of various isomorphic Ce-UiO-66-X nanozymes was carried out by a one-pot process, similar to that of Ce-UiO-66 [53–55]. The difference was that Ce-UiO-66-X (X = H, Br, NO_2, CH_3, and OH) nanozymes were assembled from Ce^{4+} and various Na_2BDC ligands with the substitution of H by NO_2, Br, CH_3, and OH, giving several white and brown (Ce-UiO-66-OH) suspensions (Fig. S6 in the ESM). The TEM images displayed uniform particles of various Ce-UiO-66-X nanozymes with similar average sizes of ~ 100 nm (Fig. 4(a)). The XRD diffraction peaks of various Ce-UiO-66-X nanozymes with different functional groups closely matched the simulated peaks for UiO-66, indicating the successful synthesis of various isomorphic Ce-UiO-66-X nanozymes (Fig. 4(b)). They also exhibited similar FTIR spectra (Fig. 4(c)). A new absorption peak of Ce-UiO-66-NO_2 at ~ 1536 cm^{-1} was observed, which was assigned to $-NO_2$ stretching vibration. Meanwhile, two characteristic peaks appear at ~ 519 and ~ 1400 cm^{-1} in the FTIR spectra of Ce-UiO-66-Br and Ce-UiO-66-CH_3, respectively, corresponding to the C–Br stretching vibration and $-CH_3$ bending vibration. For Ce-UiO-66-OH, the absorption band at ~ 1243 cm^{-1} in the FTIR spectrum was attributed to the –OH functional group. According to these results of FTIR spectra, the Ce-UiO-66-X nanozymes were successfully prepared by using Na_2BDC with different functional groups as ligands, including –H, NO_2, Br, CH_3, and OH. XPS was then employed to examine the surface chemical states of various Ce-UiO-66-X nanozymes. The percentages of Ce^{3+} in series of Ce-UiO-66-X with different functional groups were not significantly different (~ 49%), suggesting no obvious influences of the different functional groups on the valence states of cerium in Ce-UiO-66-X (Fig. 4(d) and Fig. S7 in the ESM).

Since the decisive roles of the electrostatic attraction between the catalyst and substrate in determining the adsorption capacity, zeta potential measurement was performed to analyze the surface charge states of various Ce-UiO-66-X nanozymes. The zeta potentials of Ce-UiO-66, Ce-UiO-66-Br, Ce-UiO-66-NO_2, Ce-UiO-66-CH_3, and Ce-UiO-66-OH were 25.0, 42.3, 40.2, 12.1, and −2.5 mV, respectively (Fig. 4(e)). These measurements suggested that the surface charge was significantly impacted by the different functional groups of ligands.

Thus, the surface charge of various Ce-UiO-66-X nanozymes prepared by ligands in the presence of different functional groups

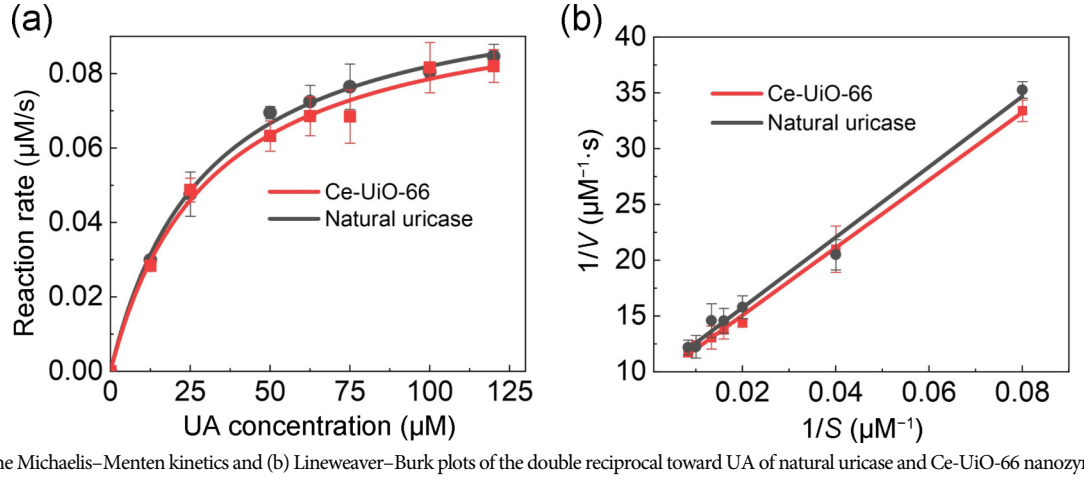

Figure 3 (a) The Michaelis–Menten kinetics and (b) Lineweaver–Burk plots of the double reciprocal toward UA of natural uricase and Ce-UiO-66 nanozyme.

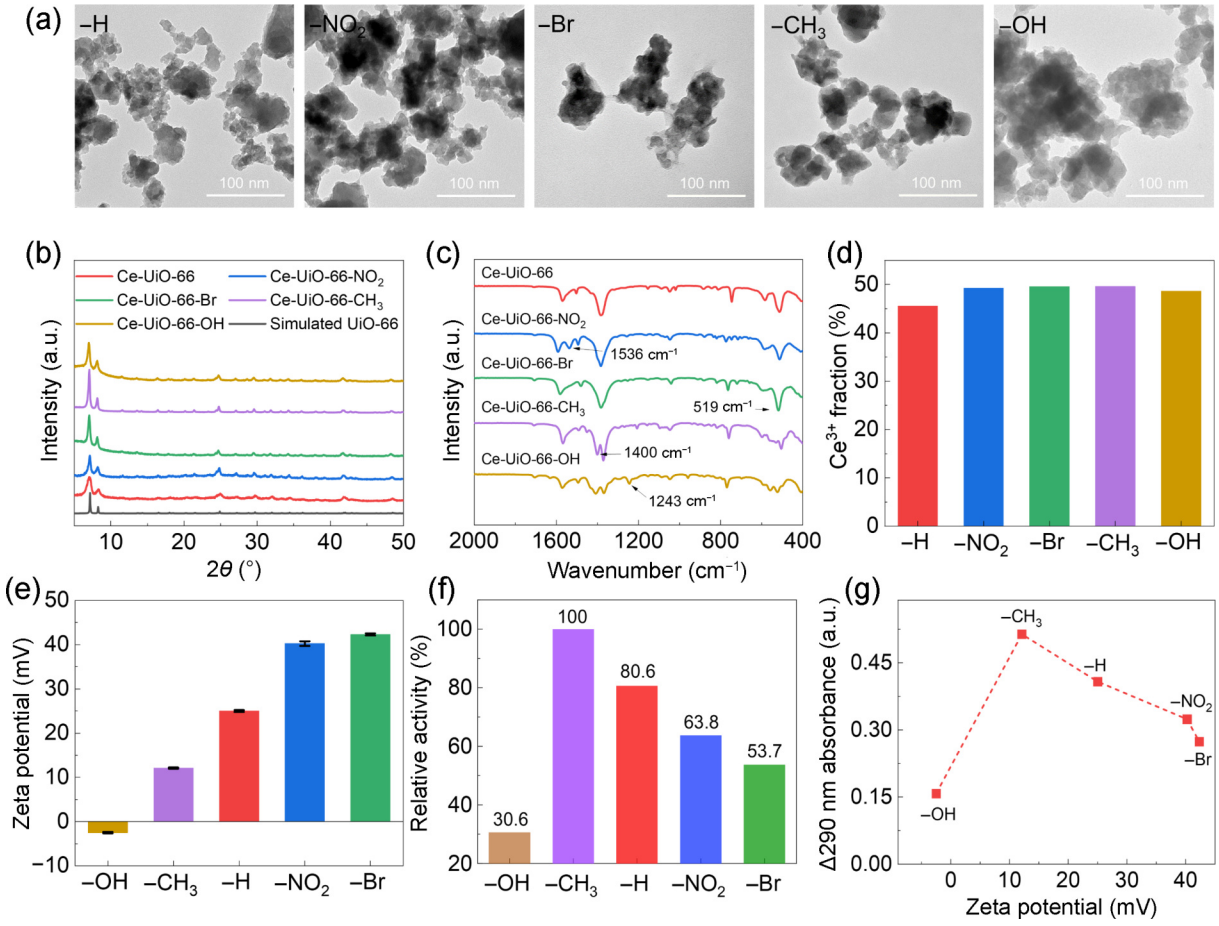

Figure 4 Characterizations of Ce-UiO-66-X (X = H, Br, NO_2, CH_3, and OH) nanozymes: (a) TEM images, (b) XRD patterns, (c) FTIR spectra, (d) Ce^{3+} fractions, and (e) zeta potentials. (f) Relative activity of Ce-UiO-66-X for the UA degradation. (g) Relationship between zeta potentials and relative activity of Ce-UiO-66-X.

could affect their uricase-like activities. Afterwards, the uricase-like activities of various Ce-UiO-66-X nanozymes were assessed (Fig. 4(f)). Compared with Ce-UiO-66, the uricase-like activity of Ce-UiO-66-CH_3 was significantly enhanced. Nevertheless, the uricase-like activity of other Ce-UiO-66-X nanozymes was lower than that of Ce-UiO-66. The sequence of uricase-like activity of various Ce-UiO-66-X nanozymes was in an order of Ce-UiO-66-CH_3 > Ce-UiO-66 > Ce-UiO-66-NO_2 > Ce-UiO-66-Br > Ce-UiO-66-OH, which might be related to the adsorption behavior of UA and allantoin on Ce-UiO-66-X. Generally, both the negatively charged UA and product allantoin molecules are more accessible to the positively charged surfaces of Ce-UiO-66-CH_3, Ce-UiO-66, Ce-UiO-66-NO_2, and Ce-UiO-66-Br rather than on Ce-UiO-66-OH. As the zeta potential increased, the uricase-like activity of Ce-UiO-66-X nanozymes increased initially and then decreased afterward, displaying a volcano-shaped profile as a function of the zeta potential of various nanozymes (Fig. 4(g)). It could be attributed to the competitive adsorption of UA and allantoin on the catalyst surfaces with different zeta potentials. With the initial increase of zeta potentials from the negative value of –2.5 mV (Ce-UiO-66-OH) to the positive value of 12.1 mV (Ce-UiO-66-CH_3), the uricase-like activity of Ce-UiO-66-X was enhanced by the increase of zeta potential of nanozymes. Afterwards, too positively charged Ce-UiO-66-X nanozymes attracted UA and also enhanced the adsorption of product allantoin due to the electrostatic effect between nanozymes and product. Therefore, the product allantoin desorption from the nanozyme surface with too positive charge became difficult, resulting in the decreased activity of Ce-UiO-66-X. Overall, Ce-UiO-66-CH_3 was chosen as the optimized nanozyme for the colorimetric sensing of UA in the subsequent experiments.

We have conducted preliminary analyses on the isothermal adsorption–desorption curve and pore size distribution of Ce-UiO-66-CH_3 (Fig. S8 and Table S2 in the ESM). Compared to Ce-UiO-66, Ce-UiO-66-CH_3 exhibits a relatively lower specific surface area and narrower pore size distribution. However, Ce-UiO-66-CH_3 demonstrates enhanced activity in the UA reaction, indicating that the surface charge state of Ce-UiO-66-X catalysts significantly influences catalytic efficiency.

3.4 Investigations on the mechanism of Ce-UiO-66-CH_3 for the colorimetric responses to UA

Our group previously developed a reagentless colorimetric smartphone analysis platform based on natural oxidase-encapsulated Ce-UiO-66 for one-step detection of various biomarkers [45]. Herein, Ce-UiO-66-CH_3 was explored for the UA detection in the absence of any natural enzymes and chromogenic agents. As shown in Fig. S9 in the ESM and Video ESM2, Ce-UiO-66-CH_3 quickly underwent a color transition from white to orange upon exposure to UA. This intriguing phenomenon prompted us to conduct a series of characterizations in order to elucidate the underlying mechanism of the color change. Obviously, compared with pristine Ce-UiO-66-CH_3, the conspicuous lattice stripes were observed in the high-resolution TEM image of the Ce-UiO-66-CH_3 treated with UA. By measuring the lattice spacing, it was concluded

that the stripes represented the (111) and (220) faces of CeO_2, respectively, demonstrating that small CeO_2 nanoclusters were indeed produced in Ce-UiO-66-CH_3 with the treatment of UA (Fig. 5(a)) [47]. Additionally, in their XRD patterns, the two main diffraction peaks located at low diffraction angles of Ce-UiO-66-CH_3 disappeared after the treatments with UA (Fig. 5(b)). While two broad diffraction peaks representing the (111) and (220) crystal planes of CeO_2 were observed in the UA-treated Ce-UiO-66-CH_3. Furthermore, as illustrated in Fig. 5(c), the UA-treated Ce-UiO-66-CH_3 nanozymes showed a strong Raman characteristic peak at 470 cm^{-1}, which was attributed to the F_{2g} symmetric vibrational mode of Ce–O in CeO_2. All phenomena demonstrated that Ce-UiO-66-CH_3 underwent a phase transition into CeO_2 after the treatment with UA, inducing the color change. Furthermore, the proportion of Ce^{3+} in the UA-pretreated Ce-UiO-66-CH_3 increased from 45% of the pristine Ce-UiO-66-CH_3 to 49%, which could be attributed to the formation of the highly defective CeO_{2-x} (Fig. 5(d)). Taking all together, the production of H_2O_2 accompanied with the catalytic oxidation of UA by Ce-UiO-66-CH_3 induced further phase transition from Ce-UiO-66-CH_3 into CeO_2. In this case, the Ce_6 core clusters in Ce-UiO-66-CH_3 were converted to CeO_2 clusters by H_2O_2, which led to the color change of Ce-UiO-66-CH_3. This exciting phenomenon opens up the possibility of the intelligent colorimetric detection of UA by Ce-UiO-66-CH_3.

3.5 Colorimetric detection platform for UA based on Ce-UiO-66-CH_3

Figure 6(a) shows the operational flow of the Ce-UiO-66-CH_3 colorimetric analysis platform for the UA detection. Ce-UiO-66-CH_3 was mixed with a solution of UA in a 96-well plate for a duration of 3 min. The color evolution of Ce-UiO-66-CH_3 was then captured via a cellphone camera in a dark box with the stable lighting conditions. Ultimately, the reaction color intensity signal was obtained by taking a picture with a smartphone and then outputted RGB values through optical image quantification by the software Visual Detection (Video ESM1), which could be further converted to the concentrations of UA by a pre-calibrated fitting curve [47, 56]. Details of the operation of software Visual Detection and quantitative analysis of colorimetric analysis by the 4-parameter logistic equation could be found in our previous report [47]. Besides, the color intensity was positively correlated with the reaction time of the UA oxidation, and the intensity increased with the increased time until it stabilized for 3 min. Therefore, the optimized detection time was set to 3 min for the real-time detection of UA (Fig. S10 in the ESM). The entire procedure is uncomplicated and rapid, enabling a real-time monitoring with high throughput. It's evident that the color of Ce-UiO-66-CH_3 changed gradually from white to orange with the increased concentrations of UA (the inset in Fig. 6(b)). The platform demonstrated the robust curvilinear relationships in detecting various concentrations of UA (Fig. 6(b)). The linear region of the concentrations of UA ranged from 31 to 4000 μM, giving a fitting equation of $y = 222.4 - 130.9/(1 + (\lg C_{UA}/2.48)^{10.82})$ ($R^2 = 0.9999$) and a LOD of 8.9 μM [53]. Compared to previously reported assays (Fig. 6(c) and Table S3 in the ESM), this colorimetric bioanalytical platform demonstrated significant advantages in terms of high-throughput screening, wide detection range, and high assay sensitivity [58–64].

Considering the exceptional performance, it was deemed necessary to conduct a further evaluation of the stability of Ce-UiO-66-CH_3 colorimetric analysis platform. Initially, the colorimetric performance of Ce-UiO-66-CH_3 was evaluated and examined at various temperatures. As shown in Fig. S11(a) in the ESM, the colorimetric platform exhibited excellent detection stability in the temperature range of 0–60 °C, indicating its high capability for reliable detection and analysis under various temperatures. Notably, the colorimetric platform based on Ce-UiO-66-CH_3 had stable colorimetric analysis performance (> 70%) over a wide range of pH at 4–8, offering a facile methodology for one-step UA detection under neutral conditions (Fig. S11(b) in the ESM). In addition, Ce-

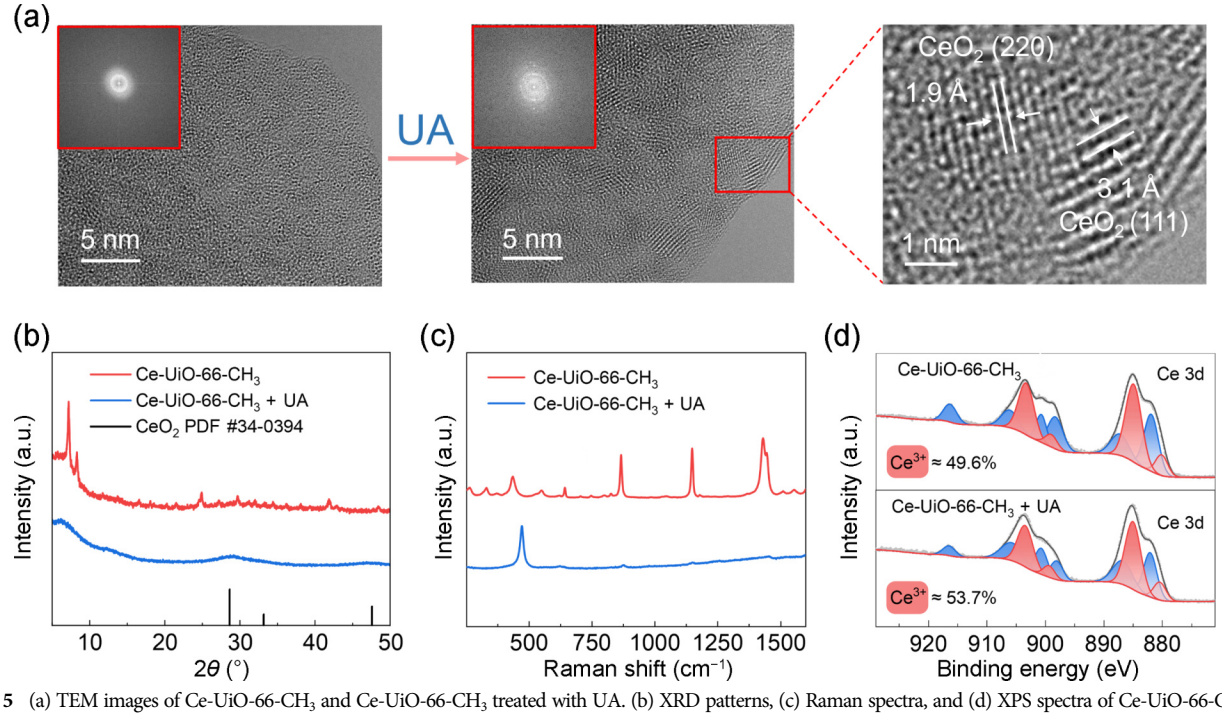

Figure 5 (a) TEM images of Ce-UiO-66-CH_3 and Ce-UiO-66-CH_3 treated with UA. (b) XRD patterns, (c) Raman spectra, and (d) XPS spectra of Ce-UiO-66-CH_3 and UA-treated Ce-UiO-66-CH_3.

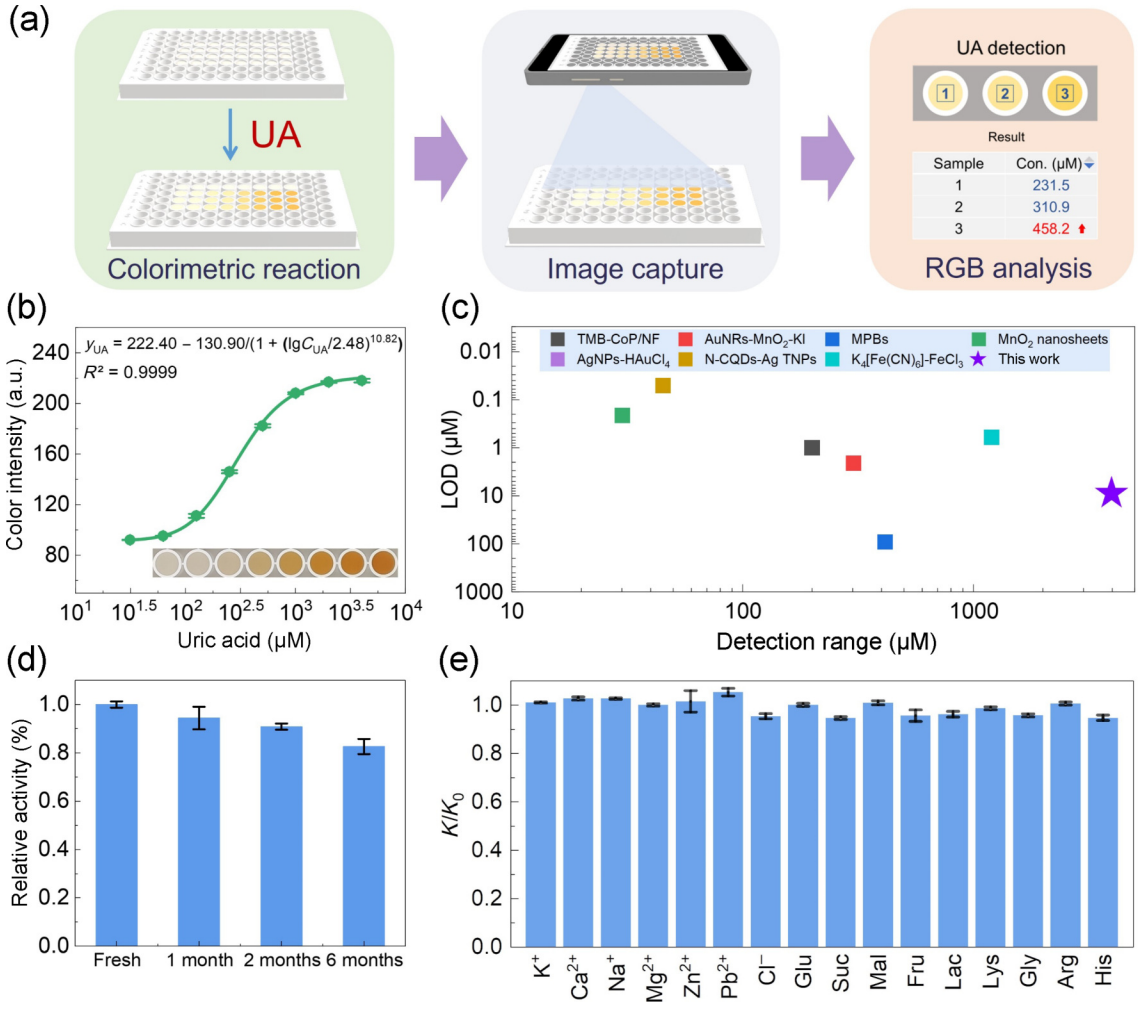

Figure 6 (a) The operational flow of the Ce-UiO-66-CH_3 colorimetric analysis platform for the UA detection. (b) Curvilinear relationship between colorimetric intensity and UA concentration in the detection system. (c) Comparison of the LOD and detection range of Ce-UiO-66-CH_3 and various previous nanozymes [54–60]. (d) Catalytic stability of Ce-UiO-66-CH_3 after storage for different periods. (e) Plot of the anti-interference level of the colorimetric detection platform with the addition of various interfering ions and amino acids. For the comparison, the color intensity obtained by detecting UA without interfering substances was denoted K_0, while the color intensity measured in the presence of interfering substances was denoted K.

UiO-66-CH_3 exhibited an excellent storage stability, as evidenced by the maintained activity levels above 80% even after six months of storage at room temperature (Fig. 6(d)). Subsequently, we added common interfering substances (various ions and amino acids) to the samples to be tested, and then evaluated the platform's response to the detection of UA in the presence of various common interfering substances in body fluids [65, 66]. As shown in Fig. 6(e), Ce-UiO-66-CH_3 delivered a high selectivity for the detection of UA and was barely affected by common interfering substances, illustrating the potentials of the colorimetric platform based on Ce-UiO-66-CH_3 for the accurate detection of UA in a complex biological sample.

Finally, to verify the potentials of the Ce-UiO-66-CH_3-based platform for practical applications, this colorimetric assay platform was further compared with the commercially available kits by serum samples. As shown in Table S4 in the ESM, the recovery of the UA concentration by Ce-UiO-66-CH_3 (100%–104%) was superior to that of the commercial kits (93%–101%) in the serum samples [57]. Finally, two human serum samples were selected for spiked recovery experiments to verify the accuracy of this Ce-UiO-66-CH_3-based platform. As shown in Table S5 in the ESM, the recovery of UA ranged from 95.2% to 109.5% with the relative standard deviation (RSD) below 2.3%. The aforementioned results suggest that the Ce-UiO-66-CH_3 platform is highly dependable in its measurements. Overall, this colorimetric platform exhibits high temperature and storage stability, enabling easy and rapid colorimetric detection of UA with high throughput, high sensitivity, and wide range. The detection platform also offers good immunity to various interferences, showing its potentials to be commercialized.

4 Conclusions

In summary, the uricase-like activity of series of Ce-UiO-66-X nanozymes was modulated by the surface charge through ligand regulation strategy, which showed promises as a smartphone-assisted all-in-one analysis platform featured with enzyme/reagent-free, rapid, sensitive, and selective sensing of UA. Compared with previous reports of detecting UA through conventional methods, this Ce-UiO-66-X nanozymes-based analysis platform does not rely on various expensive instruments and natural uricase as well as toxic and unstable chromogenic agents, offering a facile methodology for one-step UA detection. On the basis of this

enzyme/reagent-free sensing strategy, a smartphone-assisted platform has been successfully developed for sensitive (LOD: 8.9 μM), rapid (~ 3 min), and precise visual detection of UA with high anti-interference ability. Meanwhile, no deterioration in the capability of the UA detection system after storage of 6 months further demonstrated their structural and activity stability for practical application ability for the cost-effective and on-site clinical UA detection.

Electronic Supplementary Material: Supplementary material (UV–vis absorption spectra, standard curve of the UA, FTIR spectra, XPS spectra, adsorption/desorption curves, pore size distribution and colorimetric stability) is available in the online version of this article at https://doi.org/10.26599/NR.2025.94907115.

Data availability

All data needed to support the conclusions in the paper are presented in the manuscript and the Electronic Supplementary Material. Additional data related to this paper may be requested from the corresponding author upon request.

Acknowledgements

This work was supported by the National Key Research and Development Program of China (No. 2021YFB3500904), the National Natural Science Foundation of China (No. 22475173), and the Key Research and Development Program of Shaanxi (No. 2024SF-YBXM-439). Authors also acknowledge the support from Fundamental Research Funds for the Central Universities (No. D5000210635).

Declaration of competing interest

All the contributing authors report no conflict of interests in this work.

Author contribution statement

Z. X. G.: Data curation, writing manuscript, experimental design. D. C.: Data curation, writing manuscript. W. G.: Project administration, writing manuscript. Y. Q. Q.: Project administration, funding acquisition, writing manuscript. Z. M. T.: Project administration, funding acquisition, writing manuscript. All the authors have approved the final manuscript.

Use of AI statement

None.

References

[1] Rees, F.; Hui, M.; Doherty, M. Optimizing current treatment of gout. *Nat. Rev. Rheumatol.* **2014**, *10*, 271–283.

[2] Alvarez-Lario, B.; Macarron-Vicente, J. Uric acid and evolution. *Rheumatology* **2010**, *49*, 2010–2015.

[3] Dehlin, M.; Jacobsson, L.; Roddy, E. Global epidemiology of gout: Prevalence, incidence, treatment patterns and risk factors. *Nat. Rev. Rheumatol.* **2020**, *16*, 380–390.

[4] Martinon, F.; Pétrilli, V.; Mayor, A.; Tardivel, A.; Tschopp, J. Gout-associated uric acid crystals activate the NALP3 inflammasome. *Nature* **2006**, *440*, 237–241.

[5] Feig, D. I.; Kang, D. H.; Johnson, R. J. Uric acid and cardiovascular risk. *N. Engl. J. Med.* **2008**, *359*, 1811–1821.

[6] Terkeltaub, R. Update on gout: New therapeutic strategies and options. *Nat. Rev. Rheumatol.* **2010**, *6*, 30–38.

[7] Zhou, R. B.; Tardivel, A.; Thorens, B.; Choi, I.; Tschopp, J. Thioredoxin-interacting protein links oxidative stress to inflammasome activation. *Nat. Immunol.* **2010**, *11*, 136–140.

[8] Kim, J.; Imani, S.; De Araujo, W. R.; Warchall, J.; Valdés-Ramírez, G.; Paixão, T. R. L. C.; Mercier, P. P.; Wang, J. Wearable salivary uric acid mouthguard biosensor with integrated wireless electronics. *Biosens. Bioelectron.* **2015**, *74*, 1061–1068.

[9] Sherman, M. R.; Saifer, M. G. P.; Perez-Ruiz, F. PEG-uricase in the management of treatment-resistant gout and hyperuricemia. *Adv. Drug Deliv. Rev.* **2008**, *60*, 59–68.

[10] Sands, E.; Kivitz, A.; DeHaan, W.; Leung, S. S.; Johnston, L.; Kishimoto, T. K. Tolerogenic nanoparticles mitigate the formation of anti-drug antibodies against pegylated uricase in patients with hyperuricemia. *Nat. Commun.* **2022**, *13*, 272.

[11] Zhang, R. F.; Jiang, B.; Fan, K. L.; Gao, L. Z.; Yan, X. Y. Designing nanozymes for *in vivo* applications. *Nat. Rev. Bioeng.* **2024**, *2*, 849–868.

[12] Huang, Y. Y.; Ren, J. S.; Qu, X. G. Nanozymes: Classification, catalytic mechanisms, activity regulation, and applications. *Chem. Rev.* **2019**, *119*, 4357–4412.

[13] Wu, J. J. X.; Wang, X. Y.; Wang, Q.; Lou, Z. P.; Li, S. R.; Zhu, Y. Y.; Qin, L.; Wei, H. Nanomaterials with enzyme-like characteristics (nanozymes): Next-generation artificial enzymes(II). *Chem. Soc. Rev.* **2019**, *48*, 1004–1076.

[14] Li, Z.; Wu, D. H.; Wang, Q. C.; Zhang, Q. X.; Xu, P.; Liu, F. N.; Xi, S. B.; Ma, D. W.; Lu, Y. Z.; Jiang, L. et al. Bioinspired homonuclear diatomic iron active site regulation for efficient antifouling osmotic energy conversion. *Adv. Mater.*, in press, https://doi.org/10.1002/adma.202408364.

[15] Li, Z.; Liu, F. N.; Chen, C. X.; Jiang, Y. Y.; Ni, P. J.; Song, N. N.; Hu, Y.; Xi, S. B.; Liang, M. M.; Lu, Y. Z. Regulating the N coordination environment of Co single-atom nanozymes for highly efficient oxidase mimics. *Nano Lett.* **2023**, *23*, 1505–1513.

[16] Xu, J. X.; Wu, M. J.; Yang, J.; Zhao, D. Z.; He, D.; Liu, Y. J.; Yan, X.; Liu, Y. Y.; Pu, D. J.; Tan, Q. Y. et al. Multimodal smart systems reprogramme macrophages and remove urate to treat gouty arthritis. *Nat. Nanotechnol.* **2024**, *19*, 1544–1557.

[17] Dong, Y. Q.; Chi, Y. W.; Lin, X. M.; Zheng, L. Y.; Chen, L. C.; Chen, G. N. Nano-sized platinum as a mimic of uricase catalyzing the oxidative degradation of uric acid. *Phys. Chem. Chem. Phys.* **2011**, *13*, 6319–6324.

[18] Xi, J. Q.; Zhang, R. F.; Wang, L. M.; Xu, W.; Liang, Q.; Li, J. Y.; Jiang, J.; Yang, Y. L.; Yan, X. Y.; Fan, K. L. et al. A nanozyme-based artificial peroxisome ameliorates hyperuricemia and ischemic stroke. *Adv. Funct. Mater.* **2021**, *31*, 2007130.

[19] Lin, A. Q.; Sun, Z. Y.; Xu, X. Q.; Zhao, S.; Li, J. W.; Sun, H.; Wang, Q.; Jiang, Q.; Wei, H.; Shi, D. Q. Self-cascade uricase/catalase mimics alleviate acute gout. *Nano Lett.* **2022**, *22*, 508–516.

[20] Wang, K. Y.; Hong, Q.; Zhu, C. X.; Xu, Y.; Li, W.; Wang, Y.; Chen, W. H.; Gu, X.; Chen, X. H.; Fang, Y. F. et al. Metal-ligand dual-site single-atom nanozyme mimicking urate oxidase with high substrates specificity. *Nat. Commun.* **2024**, *15*, 5705.

[21] Xi, Z.; Xie, J.; Hu, J.; Wang, Q. C.; Wang, Z. Y.; Yang, X. Q.; Zong, L. Y.; Zhang, M. Y.; Sun, X. H.; Sun, S. H. et al. Polyvinylpyrrolidone-coated cubic hollow nanocages of $PdPt_3$ and $PdIr_3$ as highly efficient self-cascade uricase/peroxidase mimics. *Nano Lett.* **2024**, *24*, 3432–3440.

[22] Hu, J.; Zhao, R. F.; Gu, J. K.; Xi, Z.; Wang, Y.; Sun, X. H.; Xu, Z. B.; Sha, K. X.; Xi, J. Q.; Liu, Y. et al. Crystal facet controlled metal–support interaction in uricase mimics for highly efficient hyperuricemia treatment. *Nano Lett.* **2024**, *24*, 6634–6643.

[23] Liu, Y.; Li, N.; Su, K.; Du, J. M.; Guo, R. Arginine-rich peptide-

rhodium nanocluster@reduced graphene oxide composite as a highly selective and active uricase-like nanozyme for the degradation of uric acid and inhibition of urate crystal. *Inorg. Chem.* **2024**, *63*, 13602–13612.

[24] Liu, D. H.; Yi, S. M.; Ni, X.; Zhang, J. J.; Wang, F. Q.; Yang, P.; Liu, M. R.; Peng, J.; Dramou, P.; He, H. Preparation and application of nanozymes with uricase-like activity based on molecularly imprinted polymers. *ChemPlusChem* **2023**, *88*, e202200286.

[25] Liu, D. H.; Yang, P.; Wang, F. Q.; Wang, C.; Chen, L.; Ye, S. J.; Dramou, P.; Chen, J. H.; He, H. Study on performance of mimic uricase and its application in enzyme-free analysis. *Anal. Bioanal. Chem.* **2021**, *413*, 6571–6580.

[26] Parmekar, M. V.; Salker, A. V. Highly tuned cobalt-doped MnO_2 nanozyme as remarkably efficient uricase mimic. *Appl. Nanosci.* **2020**, *10*, 317–328.

[27] Chen, Z.; Yu, Y. X.; Gao, Y. H.; Zhu, Z. L. Rational design strategies for nanozymes. *ACS Nano* **2023**, *17*, 13062–13080.

[28] Somerville, S. V.; Li, Q. Y.; Wordsworth, J.; Jamali, S.; Eskandarian, M. R.; Tilley, R. D.; Gooding, J. J. Approaches to improving the selectivity of nanozymes. *Adv. Mater.* **2024**, *36*, 2211288.

[29] Shen, X. M.; Wang, Z. Z.; Gao, X. J.; Gao, X. F. Reaction mechanisms and kinetics of nanozymes: Insights from theory and computation. *Adv. Mater.* **2024**, *36*, 2211151.

[30] Zheng, J. J.; Zhu, F. Y.; Song, N. N.; Deng, F.; Chen, Q.; Chen, C.; He, J. Y.; Gao, X. F.; Liang, M. M. Optimizing the standardized assays for determining the catalytic activity and kinetics of peroxidase-like nanozymes. *Nat. Protoc.*, in press, https://doi.org/10.1038/s41596-024-01034-7.

[31] Liu, B. W.; Liu, J. W. Surface modification of nanozymes. *Nano Res.* **2017**, *10*, 1125–1148.

[32] Dong, H. J.; Fan, Y. Y.; Zhang, W.; Gu, N.; Zhang, Y. Catalytic mechanisms of nanozymes and their applications in biomedicine. *Bioconjugate Chem.* **2019**, *30*, 1273–1296.

[33] Zandieh, M.; Liu, J. W. Surface science of nanozymes and defining a nanozyme unit. *Langmuir* **2022**, *38*, 3617–3622.

[34] Yang, L.; Dong, S. M.; Gai, S. L.; Yang, D.; Ding, H.; Feng, L. L.; Yang, G. X.; Rehman, Z.; Yang, P. P. Deep insight of design, mechanism, and cancer theranostic strategy of nanozymes. *Nano-Micro Lett.* **2024**, *16*, 28.

[35] Chandio, I.; Ai, Y. J.; Wu, L.; Liang, Q. L. Recent progress in MOFs-based nanozymes for biosensing. *Nano Res.* **2024**, *17*, 39–64.

[36] Li, L.; Wen, Q. L.; Wang, T.; Xiao, S. T.; Gao, Y.; Wang, M.; Xu, X. H.; Ma, L.; Cheng, C. Metal-organic frameworks-engineered reactive-oxygen catalytic materials: Enzyme-mimicking coordinations, structure evolutions, and biotherapeutic applications. *Mater. Today* **2024**, *78*, 142–180.

[37] Wang, D. D.; Jana, D.; Zhao, Y. L. Metal-organic framework derived nanozymes in biomedicine. *Acc. Chem. Res.* **2020**, *53*, 1389–1400.

[38] Ma, Y. Y.; Tian, Z. M.; Zhai, W. F.; Qu, Y. Q. Insights on catalytic mechanism of CeO_2 as multiple nanozymes. *Nano Res.* **2022**, *15*, 10328–10342.

[39] Kim, Y. G.; Lee, Y.; Lee, N.; Soh, M.; Kim, D.; Hyeon, T. Ceria-based therapeutic antioxidants for biomedical applications. *Adv. Mater.* **2024**, *36*, 2210819.

[40] Wang, T. T.; Guo, W. F.; Lv, X. X.; Li, H. R.; Zhou, L.; Feng, L.; Xia, D.; Han, X.; Wang, Q.; Qu, Y. Q. et al. Catalytically self-supplied oxygen to alleviate hypoxia for treatment of acute kidney injury. *Adv. Funct. Mater.* **2024**, *34*, 2404774.

[41] Xu, K. Q.; Cheng, Y.; Yan, J.; Feng, Y. L.; Zheng, R. X.; Wu, X. Q.; Wang, Y. J.; Song, P. P.; Zhang, H. Y. Polydopamine and ammonium bicarbonate coated and doxorubicin loaded hollow cerium oxide nanoparticles for synergistic tumor therapy. *Nano Res.* **2019**, *12*, 2947–2953.

[42] Dong, S. M.; Dong, Y. S.; Jia, T.; Liu, S. K.; Liu, J.; Yang, D.; He, F.; Gai, S. L.; Yang, P. P.; Lin, J. GSH-depleted nanozymes with hyperthermia-enhanced dual enzyme-mimic activities for tumor nanocatalytic therapy. *Adv. Mater.* **2020**, *32*, 2002439.

[43] Weng, Q. J.; Sun, H.; Fang, C. Y.; Xia, F.; Liao, H. W.; Lee, J.; Wang, J. C.; Xie, A.; Ren, J. F.; Guo, X. et al. Catalytic activity tunable ceria nanoparticles prevent chemotherapy-induced acute kidney injury without interference with chemotherapeutics. *Nat. Commun.* **2021**, *12*, 1436.

[44] Huang, Y. K.; Zhang, M. Z.; Jin, M. D.; Ma, T. F.; Guo, J. L.; Zhai, X. Y.; Du, Y. P. Recent advances on cerium oxide-based biomaterials: Toward the next generation of intelligent theranostics platforms. *Adv. Healthc. Mater.* **2023**, *12*, 2300748.

[45] Yao, C.; Xu, Y. W.; Tang, J. P.; Hu, P.; Qi, H. D.; Yang, D. Y. Dynamic assembly of DNA-ceria nanocomplex in living cells generates artificial peroxisome. *Nat. Commun.* **2022**, *13*, 7739.

[46] Liu, C.; Gui, L.; Zheng, J. J.; Xu, Y. Q.; Song, B. L.; Yi, L.; Jia, Y. J.; Taledaohan, A.; Wang, Y. J.; Gao, X. F. et al. Intrinsic strain-mediated ultrathin ceria nanoantioxidant. *J. Am. Chem. Soc.* **2023**, *145*, 19086–19097.

[47] Guo, Z. X.; Tian, Z. M.; Qu, Y. Q. One-step reagentless colorimetric analysis platform of biomineralized Ce-UiO-66 for universal detection of biomarkers. *Sens. Actuators B: Chem.* **2023**, *397*, 134705.

[48] Luan, X. W.; Pan, Y. C.; Zhou, D. T.; He, B. S.; Liu, X. L.; Gao, Y. F.; Yang, J. J.; Song, Y. J. Cerium metal organic framework mediated molecular threading for point-of-care colorimetric assays. *Biosens. Bioelectron.* **2020**, *165*, 112406.

[49] Xia, C. Q.; Zhang, X. M.; Liu, X. T.; Wu, D. H.; Guo, L. Q. Old dogs, new trick: Classical starch-sodium iodide reagent as the chromogenic substrate of peroxidase-like nanozymes. *Sens. Actuators B: Chem.* **2022**, *368*, 132229.

[50] Li, Y. Y.; Zeng, Z. H.; Tong, J. J.; Yang, T.; Liu, G. H.; Feng, B.; Zhang, P.; Liu, X. F.; Qing, T. Surface ligand-regulated nanointerfaces: Enhancing the catalytic activity and selectivity of platinum nanozymes for biomedical applications. *Appl. Surf. Sci.* **2024**, *655*, 159695.

[51] Chiu, Y. C.; Hsu, T. S.; Huang, C. Y.; Hsu, C. H. Molecular elucidation of a urate oxidase from *Deinococcus radiodurans* for hyperuricemia and gout therapy. *Int. J. Mol. Sci.* **2021**, *22*, 5611.

[52] Kahn, K.; Serfozo, P.; Tipton, P. A. Identification of the true product of the urate oxidase reaction. *J. Am. Chem. Soc.* **1997**, *119*, 5435–5442.

[53] Yang, Q. H.; Wang, Y. M.; Tang, X.; Zhang, Q. J.; Dai, S.; Peng, H. T.; Lin, Y. C.; Tian, Z. Q.; Lu, Z. Y.; Chen, L. Ligand defect density regulation in metal-organic frameworks by functional group engineering on linkers. *Nano Lett.* **2022**, *22*, 838–845.

[54] Jiang, X. Z.; Wang, W.; Tang, J. C.; Han, M.; Xu, Y. C.; Zhang, L. C.; Wu, J.; Huang, Y. Y.; Ding, Z. Y.; Sun, H. W. et al. Ligand-screened cerium-based MOF microcapsules promote nerve regeneration via mitochondrial energy supply. *Adv. Sci.* **2024**, *11*, 2306780.

[55] Wu, J. J. X.; Yu, Y. J.; Cheng, Y.; Cheng, C. Q.; Zhang, Y. H.; Jiang, B.; Zhao, X. Z.; Miao, L. Y.; Wei, H. Ligand-dependent activity engineering of glutathione peroxidase-mimicking MIL-47(V) metal-organic framework nanozyme for therapy. *Angew. Chem., Int. Ed.* **2021**, *60*, 1227–1234.

[56] Ma, C. Y.; Jiang, N.; Sun, X. Y.; Kong, L. B.; Liang, T.; Wei, X. W.; Wang, P. Progress in optical sensors-based uric acid detection. *Biosens. Bioelectron.* **2023**, *237*, 115495.

[57] Wu, H. J.; Liu, J.; Chen, Z. Y.; Lin, P. C.; Ou, W. T.; Wang, Z. A.; Xiao, W.; Chen, Y.; Cao, D. L. Mechanism and application of surface-charged ferrite nanozyme-based biosensor toward colorimetric detection of L-cysteine. *Langmuir* **2022**, *38*, 8266–8279.

[58] He, Y. F.; Qi, F.; Niu, X. H.; Zhang, W. C.; Zhang, X. F.; Pan, J. M. Uricase-free on-demand colorimetric biosensing of uric acid enabled by integrated CoP nanosheet arrays as a monolithic peroxidase mimic. *Anal. Chim. Acta* **2018**, *1021*, 113–120.

[59] Qin, X.; Yuan, C. L.; Geng, G. X.; Shi, R.; Cheng, S. Q.; Wang, Y. L. Enzyme-free colorimetric determination of uric acid based on inhibition of gold nanorods etching. *Sens. Actuators B: Chem.* **2021**, *333*, 129638.

[60] Li, N. S.; Chen, Y. T.; Hsu, Y. P.; Pang, H. H.; Huang, C. Y.; Shiue, Y. L.; Wei, K. C.; Yang, H. W. Mobile healthcare system based on the combination of a lateral flow pad and smartphone for rapid detection of uric acid in whole blood. *Biosens. Bioelectron.* **2020**, *164*, 112309.

[61] Huang, L.; Qin, S. Y.; Xu, Y. J.; Cheng, S. Q.; Yang, J.; Wang, Y. L. Enzyme-free colorimetric detection of uric acid on the basis of MnO_2 nanosheets-mediated oxidation of 3,3 ′,5,5 ′ -tetramethylbenzidine. *Microchem. J.* **2023**, *190*, 108719.

[62] Li, L.; Wang, J. L.; Chen, Z. B. Colorimetric determination of uric acid based on the suppression of oxidative etching of silver nanoparticles by chloroauric acid. *Microchim. Acta* **2020**, *187*, 18.

[63] Wang, Y. Y.; Yang, Y.; Liu, W.; Ding, F.; Zhao, Q. B.; Zou, P.; Wang, X. X.; Rao, H. B. Colorimetric and fluorometric determination of uric acid based on the use of nitrogen-doped carbon quantum dots and silver triangular nanoprisms. *Microchim. Acta* **2018**, *185*, 281.

[64] Fan, K. X.; Zeng, J. Y.; Yang, C. Y.; Wang, G. L.; Lian, K.; Zhou, X. H.; Deng, Y. P.; Liu, G. Z. Digital quantification method for sensitive point-of-care detection of salivary uric acid using smartphone-assisted μPADs. *ACS Sens.* **2022**, *7*, 2049–2057.

[65] Ji, K. X.; Xia, S. Y.; Sang, X. Q.; Zeid, A. M.; Hussain, A.; Li, J. P.; Xu, G. B. Enhanced luminol chemiluminescence with oxidase-like properties of FeOOH nanorods for the sensitive detection of uric acid. *Anal. Chem.* **2023**, *95*, 3267–3273.

[66] Hazra, P.; Vadnere, S.; Mishra, S.; Halder, S.; Mandal, S.; Ghosh, P. Review on uric acid recognition by MOFs with a future in machine learning. *ACS Appl. Mater. Interfaces* **2023**, *15*, 52065–52082.